

Continental records of organic carbon isotopic composition ($^{13}\text{C}_{\text{org}}$), weathering, paleoclimate and wildfire linked to the End-Permian Mass Extinction

Lu, Jing; Zhang, Peixin; Yang, Minfang; Shao, Longyi; Hilton, Jason

Citation for published version (Harvard):

Lu, J, Zhang, P, Yang, M, Shao, L & Hilton, J 2020, 'Continental records of organic carbon isotopic composition ($^{13}\text{C}_{\text{org}}$), weathering, paleoclimate and wildfire linked to the End-Permian Mass Extinction', *Chemical Geology*.

[Link to publication on Research at Birmingham portal](#)

General rights

Unless a licence is specified above, all rights (including copyright and moral rights) in this document are retained by the authors and/or the copyright holders. The express permission of the copyright holder must be obtained for any use of this material other than for purposes permitted by law.

- Users may freely distribute the URL that is used to identify this publication.
- Users may download and/or print one copy of the publication from the University of Birmingham research portal for the purpose of private study or non-commercial research.
- User may use extracts from the document in line with the concept of 'fair dealing' under the Copyright, Designs and Patents Act 1988 (?)
- Users may not further distribute the material nor use it for the purposes of commercial gain.

Where a licence is displayed above, please note the terms and conditions of the licence govern your use of this document.

When citing, please reference the published version.

Take down policy

While the University of Birmingham exercises care and attention in making items available there are rare occasions when an item has been uploaded in error or has been deemed to be commercially or otherwise sensitive.

If you believe that this is the case for this document, please contact UBIRA@lists.bham.ac.uk providing details and we will remove access to the work immediately and investigate.

1 Continental records of organic carbon isotopic composition ($\delta^{13}\text{C}_{\text{org}}$),
2 weathering, paleoclimate and wildfire linked to the End-Permian Mass
3 Extinction

4

5 Jing LU^{a*}, Peixin ZHANG^a, Minfang YANG^b, Longyi SHAO^a, Jason HILTON^c

6

7 ^a *State Key Laboratory of Coal Resources and Safe Mining, College of Geoscience and Surveying
8 Engineering, China University of Mining and Technology, Beijing 100083, PR China*

9 ^b *Petroleum Exploration and Development Research Institute, PetroChina, Beijing 100083, PR China*

10 ^c *School of Geography, Earth and Environmental Sciences, The University of Birmingham,
11 Edgbaston, Birmingham B15 2TT, UK*

12

13

14 * Corresponding author at: State Key Laboratory of Coal Resources and Safe Mining, College of
15 Geoscience and Surveying Engineering, China University of Mining and Technology, Beijing
16 100083, P. R. China

17

18 E-mail address: lujing@cumtb.edu.cn

19

20 ABSTRACT

21 The late Permian was the acme of Pangea assembly, with collision and subduction of global plates
22 accompanied by major changes in atmospheric composition, paleoclimates and paleoenvironments of
23 the Earth's surface system. These events are extensively recorded in marine successions from the
24 Tethys, but much less are known from continental successions that typically lack high-resolution
25 stratigraphic control. In order to reveal these fluctuations in terrestrial strata and their relationship
26 with the End-Permian Mass Extinction (EPME), we investigate continental $\delta^{13}\text{C}_{\text{org}}$, mercury and
27 nickel concentrations, wildfire, and climate change proxies from the late Permian Changhsingian
28 stage to Early Triassic Induan stage in the Yuzhou coalfield in the North China Plate (NCP). Results
29 show two negative organic carbon isotope excursions (CIE) within the Changhsingian aged
30 Sunjiagou Formation, the first (CIE-I, 2.2‰) during mid-Changhsingian and a second, larger,
31 excursion (CIE-II, 2.7‰) near the end of the Changhsingian that coincides with the peaks in the
32 Chemical Index of Alteration (CIA) value and extinction of plant species. We infer CIE-II to be the
33 global negative excursion of $\delta^{13}\text{C}_{\text{org}}$ associated with the EPME. Arid climates prevailed in the study
34 area from the Changhsingian to the early Induan inferred from the low kaolinite contents and weak
35 continental weathering, except for two short-duration episodes with higher humidity that correspond
36 with CIE-I and CIE-II. Extremely high fusinite content ($\bar{x} = 63.1\%$) and its increasing abundance
37 through the Changhsingian indicates that frequent wildfires may have been a direct cause for both
38 the destruction of terrestrial vegetation ecosystems and the rapid decline of terrestrial biodiversity at
39 the EPME. We consider that terrestrial ecosystems may have played an important role in the
40 extinction of marine communities at the EPME. This represents the first time the EMPE has been
41 demonstrated in the NCP based on combined evidence from negative carbon isotope excursion,
42 concurrent weathering trends, Ni/Al ratio and biotic extinctions, representing an important step in
43 accurately identifying and correlating the EPME in continental settings from the NCP.

44

45 **Keywords:** terrestrial strata, organic carbon isotope composition, weathering, palaeoclimate, wildfire,
46 End-Permian Mass Extinction, North China Plate

47

48 **1. Introduction**

49 The End-Permian Mass Extinction (EPME) represents the largest mass extinction event in Earth
50 history, and resulted in substantial loss of 90% marine and 70% terrestrial species (Erwin, 1994). The
51 extinction was related to extreme fluctuations in atmospheric composition, paleoclimates and
52 paleoenvironments on the Earth's surface system, that included rapid and sustained global warming
53 (Joachimski et al., 2012; Sun et al., 2012), ocean anoxia (Wignall and Twitchett, 1996) and
54 widespread wildfires (Shen et al., 2011; Chu et al., 2020) amongst other kill mechanisms (Bond and
55 Grasby, 2017). Although the underlying triggers and extinction mechanisms for the EPME are
56 complex and difficult to disentangle from each other (Bond and Grasby, 2017; Wignall et al., 2020),
57 it is generally considered that the deterioration of global climate and environment is related to
58 intense volcanic activity from the Siberian Traps during the Permian–Triassic (P–T) transition (Shen
59 et al., 2011; Burgess and Bowring, 2015; Ernst and Youbi, 2017).

60 Studies linking the EPME to changes in global climate and environment primarily focus on
61 marine strata (Wignall and Hallam, 1992; Wignall and Twitchett, 1996; Grasby and Beauchamp,
62 2009; Shen et al., 2011, 2013; Grasby et al., 2013, 2016; Liao et al., 2016, 2020) due to their often
63 continuous deposition and well-dated stratigraphic frameworks. By contrast, fewer studies have
64 focused on contemporaneous continental conditions despite their obvious link to the EPME as a
65 major source of nutrients flushed into marine settings (Algeo et al., 2013; Wignall et al., 2020). At
66 the same time ocean hypoxia thought to be triggered by algal and cyanobacterial proliferation in
67 surface waters is a common phenomenon accompanied by the extinction of marine life (e.g., Xie,
68 2007). However, the reason for cyanobacterial proliferation is controversial. Some studies have
69 attributed it to increased terrestrial input of nutrients caused by enhanced continental weathering (e.g.,

70 Algeo and Twitchett, 2010) with post-EPME oceans having high bioproductivity (e.g., Meyer, 2011;
71 Shen et al., 2015). In contrast, other studies consider it may result from the transformation of
72 nitrogen into ammonium in anoxic environments (Sun et al., 2019), with the role of land-sourced
73 nutrients limited and oceanic primary productivity low (Grasby et al., 2016a, 2019a; Sun et al., 2019).
74 Therefore, contemporaneous continental strata are important to understand the relationship of climate,
75 weathering and environmental changes between continents and marine settings.

76 From the P–T transition interval in the NCP, numerous past studies have focused on stratigraphy,
77 sedimentology, palaeontology and tectonics (e.g., Wang and Wang, 1986; Hou and Ouyang, 2000;
78 Chu et al., 2015, 2017, 2019; Zhao et al., 2017), making these continental strata ideal for evaluating
79 climate and environmental changes during this time period. These have identified major changes in
80 terrestrial diversity including extinctions in conchostracans and ostracoda (Chu et al., 2015), as well
81 as a dramatic reduction in plant species diversity near the boundary of the Changshingian aged
82 Sunjiagou Formation and Induan aged Liujiagou Formation (Chu et al., 2015, 2019). In recent years,
83 elevated mercury and nickel levels as a signature for volcanism have been documented in marine and
84 terrestrial sediments associated with the EPME (Sanei et al., 2012; Grasby et al., 2013, 2015, 2016b;
85 2019b; Burgess and Bowring, 2015; Rampino et al., 2017; Fielding et al., 2019; Shen J et al., 2019;
86 Chu et al., 2020), but elevated mercury and nickel levels have not previously been recorded in the
87 continental environments of the NCP.

88 Using the ZK21-1 borehole core in the Yuzhou Coalfield of the southern NCP, we consider
89 fluctuations in $\delta^{13}\text{C}_{\text{org}}$, mercury and nickel concentrations, clay mineral components, Mineralogical
90 Index of Alteration (MIA) for sandstones, the Chemical Index of Alteration (CIA) for mudstones,
91 and kerogen macerals to evaluate the changes of global carbon cycle, volcanism, climate, continental
92 weathering trend and wildfires in relation to the EPME. This represents an important step in the
93 application of these proxies to evaluate the Permian-Triassic boundary interval in the continental
94 successions of the NCP.

95 **2. Geological background**

96 During early Lopingian period, the NCP, surrounded by the Inner Mongolia uplift (IMU) to the
97 north and the North Qinling Belt (NQB, or Funiu paleo-land) to the south, was located in the
98 northeastern margin of the Paleo-Tethys Ocean (Fig. 1a), with a latitude of approximately 20° N
99 (Ziegler et al., 1997; Shang, 1997; Li, 2006; Muttoni et al., 2009). It was separated from the South
100 China Plate by the Paleo-Tethys Ocean, and from the Mongolian plate by the paleo-Asian ocean
101 (Zhao et al., 2017; Fig. 1a, e). During this period, sediments were mainly sourced from the northern
102 IMU for the ongoing southward subduction of the paleo-Asian Ocean beneath the NCP (Zhang et al.,
103 2014). In the Changhsingian stage, the NQB begin to uplift and became the secondary provenance of
104 the NCP, but the main provenance for the study area in the Yuzhou coalfield located in the southern
105 NCP (Shang, 1997). The main part of the NQB is represented by the Qinling Group consisting
106 predominantly of Precambrian basement units including gneiss and amphibolite (Zhang et al., 1995;
107 Dong and Santosh, 2016).

108 The stratigraphic succession, rock types and fossil plant assemblages from the late Permian to
109 Early Triassic in the study area are shown in Figure 2. The strata studied in this paper conformably
110 overlie the Upper Shihezi Formation and comprise the Sunjiagou Formation and the lower part of the
111 overlying Liujiagou Formation. The Sunjiagou Formation has been divided into three members
112 according to their lithological association (Yang and Lei, 1987; Wang, 1997). The lower and middle
113 members of the Sunjiagou Formation are composed of medium-coarse, feldspathic quartz sandstone
114 and thin layers of siltstone and mudstone, while the upper part of the Sunjiagou Formation is
115 composed only of thin layers of mudstone and siltstone, all deposited in a shore-shallow lake
116 environment (Guo et al., 1991). Based on spore-pollen and plant fossil assemblages, previous studies
117 have assigned the Sunjiagou Formation to the Changhsingian stage, and the conformably overlying
118 Liujiagou Formation to the early Early Triassic Induan stage (Wang and Wang, 1986; Hou and
119 Ouyang, 2000; Wang and Chen, 2001; Chu et al., 2015). The Liujiagou Formation mainly

120 encompasses thickly layered medium to coarse sandstone, fine-grained sandstones and siltstones
121 with few trace fossils, mainly deposited in a braided river sedimentary system. The base of its
122 lowermost Jindoushan Sandstone member has been regarded as a regional marker for the
123 Permian-Triassic boundary (Guo et al., 1991; Fig. 2d). Within the Yuzhou Coalfield, we studied
124 borehole ZK21-1 that lies within the Putaosi exploration area that is a monoclinical structure inclined
125 toward the southwest (Fig. 1b, c, d).

126

127 **3. Materials and methods**

128 From the ZK21-1 borehole in the Yuzhou coalfield, fresh sandstone (27 samples) and mudstone
129 (22 samples), were collected from the Sunjiagou Formation to the lower part of the Liujiagou
130 Formation. Sampling locations are shown in Figure 3. Every mudstone sample was first broken down
131 to less than 1 mm and then divided into two parts. One part was prepared for kerogen enrichment and
132 identification according to the China national standard (SY/T5125-2014), with no less than 300
133 effective points per sample analyzed. The remaining part of each mudstone sample was further
134 crushed below 200 mesh and divided into six subparts for (1) $\delta^{13}\text{C}_{\text{org}}$ analysis, (2) clay mineral
135 analysis, (3) Total organic content (TOC) analysis, (4) major elements analysis, (5) trace elements
136 analysis, and (6) mercury concentration analysis. Clay mineral and mercury concentration were
137 measured at the State Key Laboratory Coal Resources and Safe Mining (Beijing), and the other
138 analyses in Beijing Research Institute of Uranium Geology.

139 Organic carbon isotope analysis was performed using a stable isotope mass spectrometer
140 (MAT253), and $\delta^{13}\text{C}_{\text{org}}$ values are expressed in per mil (‰) with respect to the Vienna Pee Dee
141 Belemnite (VPDB) standard, with the absolute analysis error of $\pm 0.1\%$. Clay mineral was analyzed
142 using an X-ray diffractometer (D/max 2500 PC), and the data were interpreted using Clayquan 2016
143 software with the relative analysis error of $\pm 5\%$. Samples for TOC were first treated with phosphoric
144 acid to remove inorganic carbon, and then the TOC values were measured using a carbon-sulfur

145 analyzer (CS580-A) with the lower detection limits of 100 $\mu\text{g/g}$ and the absolute analysis error of
146 $\pm 0.2\%$. Major elements analysis was undertaken with an X-ray fluorescence spectrometer (PW2404)
147 with the relative analysis error of $\pm 5\%$. Trace elements analysis was undertaken using an inductively
148 coupled plasma mass spectrometer (Finnigan MAT) with the relative analysis error better than $\pm 5\%$.
149 Mercury concentration was undertaken using a mercury analyzer (Lumex RA-915+) with lower
150 detection limits of 2ng/g and the relative analysis error of $\pm 5\%$. More details of the analytical method
151 are described by Ma et al. (2015), Liao et al. (2016), Wu et al. (2017), Hu et al. (2020) and Chu et al.
152 (2020). Sandstone samples were cut into slices and identified by the point-counting method under a
153 microscope with more than 300 effective points of each sample. The classification of sandstone
154 components is in accordance with that of Dickinson (1985).

155 In this study, mercury and nickel concentrations have been used to indicate the presence of
156 volcanic activity due to their relationship with volcanic eruptions and magmatic intrusions (Sanei et
157 al., 2012; Burgess and Bowring, 2015; Rampino et al., 2017; Grasby et al., 2019b). The indexes of
158 MIA of sandstone and CIA of mudstone were used to restore the weathering trends of the parent rock
159 in provenance, their concepts and implications are outlined by Nesbitt and Young (1984), Fedo et al.
160 (1995), and Roy and Roser (2013). Paleoclimate inferences have been recovered by the kaolinite
161 content of mudstone, with MIA and CIA values used for reference. As the abundance of kaolinite in
162 modern sediments is dependent on the intensity of chemical weathering controlled by climate
163 (Chamley, 1989), and because of its strong diagenesis resistance, changes in its content are
164 considered to be a reliable climatic proxy (Thiry, 2000). Fusinite (Charcoal) content has been used to
165 indicate paleowildfire (e.g., Scott, 2000; Glasspool and Scott, 2010).

166

167 **4. Results**

168 *4.1. Total organic content (TOC) and distribution pattern of $\delta^{13}\text{C}_{\text{org}}$*

169 Results for TOC and $\delta^{13}\text{C}_{\text{org}}$ are shown in Table 1 and Figure 3a, b. TOC values vary from 0.05–

170 0.12 ‰ ($\bar{x} = 0.09\%$). These values are low 0.2% detection limit (see Grasby et al., 2019b) and will
171 not be used in the following discussion.

172 $\delta^{13}\text{C}_{\text{org}}$ values vary from -26.5–23.0 ‰ ($\bar{x} = -24.7\%$), and show a vertical variation trend from
173 fast negative excursion with an offset of 2.2‰ (CIE-I) in the middle of the Sunjiagou Formation,
174 followed by slow positive excursion with an offset of 1.4‰. Near the top of the Sunjiagou Formation,
175 a second, larger excursion occurs with an offset of 2.7‰ (CIE-II). After CIE-II, $\delta^{13}\text{C}_{\text{org}}$ values
176 increase at the base of the Liujiagou Formation (Fig. 3b). Vertically, CIE-I and CIE-II corresponds
177 approximately with the position of the two zones of high TOC values (Fig. 3a). High TOC values
178 occur elsewhere in the succession without corresponding $\delta^{13}\text{C}_{\text{org}}$ excursions (Fig. 3a, b).

179

180 4.2. Mercury and Nickel concentration

181 Results for mercury and nickel concentrations are shown in Table 1. Hg concentrations vary
182 from 2.21–27.04 ng/g ($\bar{x} = 22.5$ ng/g) (Table. 1) with an obvious peak in Hg concentration
183 corresponding to the position of CIE-II. Although the peak value in Hg concentration is 3 times the
184 average concentration, the value of Hg concentrations are within the average values of marine shale
185 in published papers (c.f. Grasby et al., 2019b). The nature of the Hg peak is not clear and we do not
186 regard it as definitive evidence for volcanism in the study area.

187 Nickel concentrations vary from 21.5–69.7 $\mu\text{g/g}$ ($\bar{x} = 34.45$ $\mu\text{g/g}$) with an obvious peak in
188 concentration corresponding to the position of CIE-II. The value of the peak (69.7 $\mu\text{g/g}$) is within the
189 range recorded during the P-T transition (12–800 $\mu\text{g/g}$; see Ramponi et al., 2017 and references
190 therein).

191 Although Ni concentration may be related to volcanism, some researchers consider it to be
192 influenced by aluminium content (e.g., Fielding et al., 2019). We corrected Ni concentrations by
193 aluminium concentration and the values of the Ni/Al ratio (Fig. 3e) vary from 2.36–6.72 $\times 10^{-4}$ ($\bar{x} =$
194 3.87 $\times 10^{-4}$). Two peaks in Ni/Al ratio occur of which the lower one is coincident with the position of

195 CIE-II (Fig. 3b), indicating that the peak in Ni concentration and Ni/Al ratio corresponding to CIE-II
196 is reasonable to be inferred as evidence of volcanism affecting the study area.

197

198 *4.3. Kerogen macerals*

199 Identification results of kerogen macerals are shown in Table 1 and Figure 3f. Inertinite content
200 varies from 49.3–70.1 % (\bar{x} = 63.1%) and entirely comprises fusinite (charcoal) which is opaque,
201 pure black, does not fluoresce under fluorescence illumination (Fig. 4a-c) and is usually long and
202 thin or fragmental shaped with sharp edges. Vertically through the succession, fusinite concentration
203 increases slowly at first, reaches a peak value of 70.1% near the top of the Sunjiagou Formation, and
204 then decreases slowly after entering the Liujiagou Formation. The vitrinite group, with contents
205 varying from 24.4–45.0 % (\bar{x} = 29.0%) mainly comprises normal vitrinite (Fig. 4d, e). Exinite
206 content varies from 3.6–11.9 % (\bar{x} = 7.7%) of which suberinite is the main component (Fig. 4f, g).
207 Sapropelinite content is very low with an average value of 0.3% (Fig. 4h-k).

208

209 *4.4. MIA, CIA, and Clay mineral component*

210 The values of the Th/U ratio vary from 2.04 – 4.92 (Table 3), indicating that the parent rocks of
211 the sediments in the study area are not recycled. This is because recycled mudrocks exhibit high
212 Th/U ratios of around 6 due to oxidation of U^{4+} to U^{6+} and its removal as a soluble component (c.f.
213 Bhatia and Taylor, 1981). This conclusion is consistent with the provenance properties (stable land)
214 indicated by the Dickson diagram (Fig. 5a) and is in agreement with Shang (1997) and Dong and
215 Santosh (2016) who determined sediments of the study area mainly originated from the North
216 Qinling Terrane (NQT) based on paleogeographic restoration and lithofacies analysis.

217 A reliability test of the CIA values in the study area was undertaken by the A-CN-K diagram
218 (Nesbitt and Young, 1984) that shows the CIA values deviate from the ideal weathering trend line
219 (Fig. 5b) and are affected by potassium metasomatism. Subsequently, these CIA values were

220 calibrated by the method of Fedo et al. (1995). MIA values vary from 70.9–91.8 (\bar{x} =78.8) (Table 2,
221 Fig. 3g), most of which are between 70–80 and show a relatively stable vertical distribution through
222 the succession, except for two intervals with MIA values > 80 near the middle of the Sunjiagou
223 Formation and at the boundary of the Sunjiagou and Liujiagou formations. The corrected values
224 (CIA_{corr}) vary from 78.1–86.5 (\bar{x} =83.7) (Table 3, Fig. 3h) and are similar to the MIA results,
225 reflecting moderate weathering of source area and showing a similar vertical change pattern. This
226 shows MIA and CIA are reliable indexes for indicating weathering trends in the study area. The two
227 periods of enhanced weathering approximately correspond with negative excursions CIE-I and
228 CIE-II (Fig. 3b, g, h).

229 The clay mineral components of the mudstone samples are mainly illite-smectite mixed layers,
230 followed by kaolinite and illite (Table 3, Fig. 3i, 6). The content of illite-smectite mixed layers varies
231 from 79–96 % (\bar{x} = 90.5%). Kaolinite content changes from 2–18 % (\bar{x} = 5.8%) and presents a
232 vertical trend of first decreasing and then increasing, but with two peaks in kaolinite content (about
233 10% and 18%, respectively) corresponding roughly with the position of CIE-I and CIE-II. The illite
234 content is very low with an average of 3.8%.

235

236 **5. Discussion**

237

238 *5.1. Stratigraphic correlation and the position of the EPME*

239 Previous studies of continental weathering in the Yima and Shichuanhe sections in the NCP
240 during the P-T transition shown that CIA values tends to increase first and then decrease, with the
241 maximum CIA values occurring at the top of the Sunjiagou Formation and approximately correspond
242 to the End-Permian Plant Extinction (EPPE) (Cao et al., 2019). This provide a timeline for the
243 position of the EPPE in the NCP. We follow this conclusion, using the peak in CIA as a marker for
244 the EPPE and place the EPPE at the horizon coincident with CIE-II in the study area.

245 Furthermore, chemostratigraphy can provide evidence for the correlation between the EPPE in
246 NCP and marine settings. Investigations on $\delta^{13}\text{C}$ distribution patterns from stratigraphically
247 well-constrained Lopingian to early Triassic profiles have been undertaken in marine (Meishan,
248 Niushan) (e.g., Shen et al., 2013; Liao et al., 2016, 2020) and terrestrial (Dalongkou, Lubei,
249 Guanbachong, Chahe, Longmendong, Bunnerong-1) strata (e.g., Zhang et al., 2016; Shen J et al.,
250 2019; Fielding et al., 2019). These reveal $\delta^{13}\text{C}$ is relatively stable during the early Changhsingian,
251 followed by a gradual and slow decrease during the late Changhsingian prior to a globally significant
252 excursion with an average negative offset of 3–5 ‰ shortly before the P–T boundary (Shen S et al.,
253 2019). The end-Changhsingian negative excursion of $\delta^{13}\text{C}$ represents a major reorganization of the
254 global carbon cycle associated with the EPME interval and is a global phenomenon (Shen S et al.,
255 2011, 2013, 2019).

256 In the study area, the $\delta^{13}\text{C}_{\text{org}}$ trend is very similar to that in Meishan Changhsingian stratotype
257 section at Changxing, South China (Nan and Liu, 2004). CIE-I occurs in mudstones on top of the
258 Pingdingshan Sandstone (Fig. 3), it may be a regional negative excursion as while it is present in the
259 Meishan section in South China, it is absent in many other sections globally (e.g., Yin et al., 2007).
260 In our study, no changes in plant species composition occur at this level (Fig. 2h). CIE-II occurs near
261 the top of the Sunjiagou Formation, and coincident it is a significant floral extinction event just
262 below the P-T boundary (Fig. 2h) that occurs across the NCP (Wang and Wang, 1986; Chu et al.,
263 2015). Moreover, peaks in nickel concentration and Ni/Al ratio during the P-T transition period also
264 are within the extinction interval of the EPME (Rampino et al., 2017 and references therein; Fielding
265 et al., 2019). As a result, we interpret CIE-II as correlating with the end-Changhsingian negative
266 excursion associated with the EPME in Meishan Changhsingian stratotype section. Our study
267 support the hypothesis that the extinction is synchronous in both terrestrial and marine successions
268 (Shen S et al., 2011, 2013, 2019; Zhang et al., 2016) although other recent research shows that the
269 extinction of terrestrial life earlier than that of marine life (Fielding et al., 2019; Gastaldo et al., 2020;

270 Chu et al., 2020). This might suggest that the terrestrial extinction was not synchronous, occurring
271 earlier at higher latitudes and closer or at the same time as the marine extinction at lower latitudes
272 (Feng et al., 2020).

273

274 *5.2. Paleoclimate changes and continental weathering regimes*

275 In the NCP during the Changhsingian, previous studies considered that arid paleoclimates
276 prevailed (Yang and Lei, 1987; Cope et al., 2005; Yang and Wang, 2012), related to the northward
277 drift of the NCP through arid subtropical latitudes and/or rain-shadow effect from topography
278 resulting from collision with the Mongolia block (Cope et al., 2005). In study area, the wetland
279 Cathaysian flora was rapidly succeeded by a Zechstein-type drier flora at the end of the
280 Wuchiapingian (Yang and Wang, 2012; Fig. 2g). In the NCP, the absence of coal deposition,
281 widespread distribution of red beds in the Sunjiagou and Liujiagou formations, and the occurrence of
282 calcareous nodules in the upper part of Sunjiagou Formation collectively indicate high evaporation
283 and an arid paleoclimate (Yang and Lei, 1987; Wang, 1997).

284 In our study a generally arid paleoclimate is evidenced based on low kaolinite content in
285 mudstones and the moderate-weak continental weathering of the source area (Fig. 3g, h, i, 7a).
286 However, this was not continuous with two short duration periods of relative humidity appearing in
287 the mid-Changhsingian and near the P–T boundary (Fig. 7h). This is more pronounced in the latter
288 event that coincides with CIE-II where kaolinite content of mudstones reaches 18%, and the values
289 of MIA and CIA exceed 80 and 85, respectively. This conclusion is supported by records from the
290 Yima and Shichuanhe sections in the NCP near the P–T boundary (Cao et al., 2019), where peaks in
291 CIA values roughly correspond to the EPPE. At the same time, similar peaks in CIA values and
292 Kaolinite content also were recorded in southeast Australia, the reason of which has been attributed
293 to the intensification of humidity/warmth around the EPME (Fielding et al., 2019). Short-term
294 climatic humidification and enhanced continental weathering in the P-T transition has also been

295 recorded in other areas of the world (e.g., Bachmann and Kozur, 2004; Sheldon, 2005; Retallack,
296 2005; Song, 2015).

297 There is no consensus on whether or why the climate became wet near the P–T boundary. Many
298 previous studies suggested that paleoclimate humidification around the Tethys Ocean may be related to
299 the increased precipitation and surface runoff caused by the intensification of Monsoon activity
300 (Winguth and Winguth, 2013), or acceleration of the land water cycle caused by the rising global
301 temperature (Van Soelen et al., 2018). However, some studies suggest that the increase of kaolinite
302 content and the enhancement of continental weathering from the late Changhsingian to early Induan
303 are related to the increase of atmospheric $p\text{CO}_2$ and acid rain caused by frequent volcanic activity
304 (Algeo and Twitchett, 2010; Sun et al., 2018; Cao et al., 2019). This is because elevated acidity and
305 temperature conditions can accelerate rock weathering rates. As such volcanic activity may mislead
306 the paleoclimate and continental weathering trends based on kaolinite content as well as influencing
307 MIA and CIA values.

308 In the study area, the increased kaolinite content and MIA and CIA values after the EPME
309 occurred in a period of rapidly rising global sea level (Cao et al., 2009; Yin and Song, 2013). This
310 significantly increased water vapor transportation to land (Winguth and Winguth, 2013), resulting in
311 continental climatic humidification. This may explain the terrestrial climate wetting after the EPME
312 but it cannot rule out the possibility that climate humidification and the prevalence of acid rain
313 occurred simultaneously.

314 315 *5.3. Continental Wild-fire linked to EPME and marine extinctions*

316 Fusinite, or charcoal, is fire-derived and evidences wildfires in the rock record (Scott, 2000;
317 Glasspool and Scott, 2010). In the Yuzhou coalfield, inertinite (fusinite) is the most abundant
318 kerogen maceral group ($\bar{x} = 63.1\%$). The high fusinite content and its vertical variation pattern (see
319 4.3) indicate that the paleo-fires prevailed in the southern NCP during the middle

320 Changhsingian-early Induan and reach their peak near the P–T boundary. This increasing frequency
321 of continental paleo-fires appears to be a global phenomenon, with similar records recorded in other
322 parts of NCP as well as in South China, Australia, and Canada (e.g., Wang and Chen, 2001; Grasby
323 et al., 2011; Shen et al., 2011; Chu et al., 2020).

324 Factors affecting wildfire include availability of combustible fuel, atmospheric oxygen
325 concentration to enable burning, a suitable climate lacking high moisture, and an ignition mechanism
326 (Scott, 2000). The Zechstein-type flora present across the NCP during the Changhsingian was
327 adapted for dry climates and would have been an appropriate source of fuel. Atmospheric oxygen
328 concentration at the end-Permian has been estimated as 21–27 %, far in excess of the minimum
329 oxygen requirement of 15% for plant combustion (Glasspool and Scott, 2010). Dry and hot climates
330 favor the prevalence of wildfires, and water limited conditions persisted during the Changhsingian in
331 the study area prior to the EMPE (Fig. 7h). However, at the beginning of the EPME interval, the
332 climate tended to be relatively humid reducing the likelihood of wildfire. Therefore, the prevalence
333 of wildfire in the late Changhsingian may have been controlled by ignition factors. Under natural
334 conditions, ignition is caused by lightning, volcanic eruption and less probably meteor impact
335 (Glasspool et al., 2015). Of these, there is no volcanic activity in proximity to the Yuzhou coalfield
336 suitable to ignite wildfires, nor is there any evidence for meteor impact as an ignition mechanism at
337 this time. Lightning would have been the main ignition source of wildfire in the run-up to the EPME,
338 the occurrence of which was related to the climate and atmospheric $p\text{CO}_2$ (Glasspool and Scott, 2010;
339 Glasspool et al., 2015).

340 In the NCP, wildfire may be the direct cause for both the destruction of terrestrial ecosystems
341 and the rapid decline of plant biodiversity at the EPME, also playing an important role in the
342 extinction of marine organisms (Shen et al., 2011; Zhang et al., 2016). Damage to the land surface
343 vegetation system by frequent wildfire during the EPME interval would have led to increased soil
344 erosion as well as exposing bedrock and increasing continental weathering leading to siltation (Shen

345 et al., 2011).

346 In the study area, many greyish-green and purplish red mudstone clastics occur in the lake
347 mudstone associated with the CIE-II and persist into the early Triassic in the drill core ZK21-1 (Fig.
348 8a). This is a common phenomenon in the NCP and similar mudstone clastics also was observed in
349 the uppermost Sunjiagou Formation in borehole core profile in the Liujiang area in Hebei province
350 (middle NCP) (Fig. 8b), and the Shuiyuguan section in Shaanxi Province (middle NCP) (Fig. 8c, d).
351 These mudstone clastics may indicate the increased soil erosion after the collapse of terrestrial
352 vegetation systems. This increased soil erosion does not have a significant effect on the chemical
353 weathering, because it promoted erosion and transportation of the surface soil. However, the decline
354 in CIA values following the EPPE may reflect loss of weathered soils through physical erosion (Cao
355 et al., 2019).

356 As a result of wildfire, large amounts of organic matter (including charcoal and un-charred
357 matter) and nutrients (including phosphorus and potassium) produced by plant combustion and
358 weathering of parent rock would enter the oceans through surface runoff (Algeo et al., 2013;
359 Glasspool et al., 2015). These inert organic particles would float in ocean for some time, increasing
360 oceanic turbidity through siltation, and affect the penetration of light and the photosynthesis of
361 marine organisms (Glasspool et al., 2015). Large nutrient inputs may be one of the main reasons for
362 prospering cyanobacteria and algae in oceanic surface waters (Meyer et al., 2011; Shen et al., 2015).
363 Eutrophication of seawater during the P-T transition was considered as a localized phenomenon
364 (Algeo et al., 2013) while Sun et al. (2019) considered the transformation of nitrogen to ammonium
365 the main reason for the cyanobacterial proliferation at this time. In this context, oxygen circulation
366 between seawater and atmosphere would have been inhibited by floating inert organic particles,
367 cyanobacteria and algae in surface waters, increasing the consumption of dissolved oxygen by the
368 decomposition of dead cyanobacteria and algae remains (e.g., Algeo et al., 2013; Glasspool et al.,
369 2015; Sun et al., 2019). This would have further contributed to oceanic anoxia and the extinction of

370 aerobic marine organisms.

371 While siltation may be a causal mechanism for mass extinctions in the marine realm, Wignall et
372 al. (2020) concluded this was not the case for the EPME in the western Guizhou and eastern Yunnan
373 region of the South China Plate (SCP). Plant material in that region was trapped in alluvial settings
374 during base-level rise and did not enter the ocean. However, siltation may have occurred in the
375 southeastern sea area of the NCP. Here fluvial depositional systems, represented by the Jindoushan
376 Sandstone developed through nearly the whole NCP during the P-T transition period following rapid uplift
377 of the IMU to the north (Shang, 1997; Zhang et al., 2014). Large amount of sediment including organic
378 matter may have entered the ocean from the southeast exit of the basin. Sedimentological evidence for this
379 likely siltation is not available because sedimentary strata to the west of the Tanlu Fault (Fig. 1b, c) that
380 would have recorded this were eroded post-deposition.

381

382 **6. Conclusions**

383 1) Values of $\delta^{13}\text{C}_{\text{org}}$ show negative excursions in the middle (CIE-I) and end (CIE-II)
384 Changhsingian, the latter roughly corresponds to End-Permian plant extinction (EPPE) in NCP
385 through the comparison of continental weathering trend. We infer CIE-II to be the global negative
386 excursion associated with the EPME, because it occurs in the Meishan and other sections globally,
387 and is synchronous with peaks in nickel concentration and Ni/Al ratio and with the EPPE.

388 2) Two short-duration episodes with greater humidity, corresponding to CIE-I and CIE-II
389 occurred in the context of the prevailing arid climate from the Changhsingian to the early Induan,
390 inferred from the low kaolinite content and weak continental weathering. The extremely high fusinite
391 content of kerogen macerals and their vertically increasing trend indicates that frequent wildfires
392 occurred in the run up the end Permian. Widespread and frequent wildfire is likely to have been a
393 causal mechanism for the destruction of terrestrial vegetation and ecosystems at the EPME. The
394 appearance of the mudstone clastics coincident with the CIE-II may indicate the increased soil
395 erosion after the collapse of land vegetation systems. The mudstone color shift to green may

396 indicated the development of less drained alluvial landscapes (e.g., more persistently wet), this is
397 consistent with the change in CIA values.

398

399 **Acknowledgments**

400 We thank Chu Daoliang for discussion, Sun Yadong, Donald Porcelli, Tamsin Mather, Stephen
401 Grasby and Tracy D. Frank for constructive and helpful reviews of the manuscript. Financial support
402 was provided from the National Natural Science Foundation of China (Grant no. 41472131,
403 41772161), NERC (NE/P013724/1), National Science and Technology Major Project (Award no.
404 2017ZX05009-002), and New Century Excellent Talents Fund of Chinese Ministry of Education
405 (Award no. 2013102050020).

406

407 **References**

- 408 Algeo, T.J., Henderson, C.M., Tong, J.N., Feng, Q.L., Yin, H.F., Tyson, R.V., 2013. Plankton and
409 productivity during the Permian-Triassic boundary crisis: An analysis of organic carbon fluxes.
410 *Glob. Planet. Change* 105, 52–67. <https://doi.org/10.1016/j.gloplacha.2012.02.008>
- 411 Algeo, T.J., Twitchett, R.J., 2010. Anomalous early Triassic sediment fluxes due to elevated
412 weathering rates and their biological consequences. *Geology* 38, 1023–1026.
413 <https://doi.org/10.1130/G31203.1>
- 414 Bachmann, G.H., Kozur, H.W., 2004. The Germanic Triassic: correlations with the international
415 chronostratigraphic scale, numerical ages and Milankovitch cyclicity. *Hallersches Jahrb.*
416 *Geowiss.* 26, 17–62.
- 417 Bhatia, M.R., Taylor, S.R., 1981. Trace-element geochemistry and sedimentary provinces: A study
418 from the Tasman Geosyncline, Australia. *Chem. Geol.* 33, 115–125.
419 [https://doi.org/10.1016/0009-2541\(81\)90089-9](https://doi.org/10.1016/0009-2541(81)90089-9)
- 420 Bond, D.P.G., Grasby, S.E., 2017. On the causes of mass extinctions. *Palaeogeogr. Palaeoclimatol.*
421 *Palaeoecol.* 478, 3–29. <https://doi.org/10.1016/j.palaeo.2016.11.005>
- 422 Burgess, S.D., Bowring, S.A., 2015. High-precision geochronology confirms voluminous
423 magmatism before, during, and after Earth’s most severe extinction. *Sci. Adv.* 1.
424 <https://doi.org/10.1126/sciadv.1500470>
- 425 Cao, C.Q., Love, G.D., Hays, L.E., Wang, W., Shen, S.Z., Summons, R.E., 2009. Biogeochemical
426 evidence for euxinic oceans and ecological disturbance presaging the end-Permian mass
427 extinction event. *Earth Planet. Sci. Lett.* 281, 188–201.
428 <https://doi.org/10.1016/j.epsl.2009.02.012>

- 429 Cao, Y., Song, H.Y., Algeo, T.J., Chu, D.L., Du, Y., Tian, L., Wang, Y.H., Tong, J.N., 2019.
430 Intensified chemical weathering during the Permian-Triassic transition recorded in terrestrial
431 and marine successions. *Palaeogeogr. Palaeoclimatol. Palaeoecol.* 519, 166–177.
432 <https://doi.org/10.1016/j.palaeo.2018.06.012>
- 433 Chamley, H., 1989. *Clay mineralogy*. Springer, Berlin, pp. 623.
- 434 Chu, D.L., Grasby, S.E., Song, H.J., Dal Corso, J., Wang, Y., Mather, T.A., Wu, Y., Song, H.Y., Shu,
435 W.C., Tong, J.N., Wignall, P.B., 2020. Ecological disturbance in tropical peatlands prior to
436 marine Permian-Triassic mass extinction. *Geology* 48, 288–292.
437 <https://doi.org/10.1130/g46631.1>
- 438 Chu, D.L., Tong, J.N., Benton, M.J., Yu, J.X., Huang, Y.F., 2019. Mixed continental-marine biotas
439 following the Permian-Triassic mass extinction in South and North China. *Palaeogeogr.*
440 *Palaeoclimatol. Palaeoecol.* 519, 95–107. <https://doi.org/10.1016/j.palaeo.2017.10.028>
- 441 Chu, D.L., Tong, J.N., Bottjer, D.J., Song, H.J., Song, H.Y., Benton, M.J., Tian, L., Guo, W.W.,
442 2017. Microbial mats in the terrestrial Lower Triassic of North China and implications for the
443 Permian–Triassic mass extinction. *Palaeogeogr. Palaeoclimatol. Palaeoecol.* 474, 214–231.
444 <https://doi.org/10.1016/j.palaeo.2016.06.013>
- 445 Chu, D.L., Tong, J.N., Song, H.J., Benton, M.J., Bottjer, D.J., Song, H.Y., Tian, L., 2015. Early
446 Triassic wrinkle structures on land: Stressed environments and oases for life. *Sci. Rep.* 5, 1–8.
447 <https://doi.org/10.1038/srep10109>
- 448 Cope, T., Ritts, B.D., Darby, B.J., Fildani, A., Graham, S.A., 2005. Late Paleozoic sedimentation on
449 the northern margin of the North China Block: Implications for regional tectonics and climate
450 change. *Int. Geol. Rev.* 47, 270–296. <https://doi.org/10.2747/0020-6814.47.3.270>

451 Dickinson, W.R., 1985. Interpreting provenance relations from detrital modes of sandstones. *Proven.*
452 *arenites. Proc. Cetraro, Cosenza, 1984.* https://doi.org/10.1007/978-94-017-2809-6_15

453 Dong, Y.P., Santosh, M., 2016. Tectonic architecture and multiple orogeny of the Qinling Orogenic
454 Belt, Central China. *Gondwana Res.* 29, 1–40. <https://doi.org/10.1016/j.gr.2015.06.009>

455 Ernst, R.E., Youbi, N., 2017. How Large Igneous Provinces affect global climate, sometimes cause
456 mass extinctions, and represent natural markers in the geological record. *Palaeogeogr.*
457 *Palaeoclimatol. Palaeoecol.* 478, 30–52. <https://doi.org/10.1016/j.palaeo.2017.03.014>

458 Fedo, C.M., Nesbitt, H.W., Young, G.M., 1995. Unraveling the effects of potassium metasomatism
459 in sedimentary-rocks and paleosols, with implications for paleoweathering conditions and
460 provenance. *Geology* 23, 921–924. [https://doi.org/10.1130/0091-7613\(1995\)023<0921](https://doi.org/10.1130/0091-7613(1995)023<0921)

461 Feng, Z., Wei, H.B., Guo, Y., He, X.Y., Sui, Q., Zhou, Y., Liu, H.Y., Gou, X.D., Lv, Y., 2020. From
462 rainforest to herbland: New insights into land plant responses to the end-Permian mass
463 extinction. *Earth-Science Rev.* 204, 103153. <https://doi.org/10.1016/j.earscirev.2020.103153>

464 Fielding, C.R., Frank, T.D., McLoughlin, S., Vajda, V., Mays, C., Tevyaw, A.P., Winguth, A.,
465 Winguth, C., Nicoll, R.S., Bocking, M., Crowley, J.L., 2019. Age and pattern of the southern
466 high-latitude continental end-Permian extinction constrained by multiproxy analysis. *Nat.*
467 *Commun.* 10, 385. <https://doi.org/10.1038/s41467-018-07934-z>

468 Gastaldo, R.A., Kamo, S.L., Neveling, J., Geissman, J.W., Looy, C. V., Martini, A.M., 2020. The
469 base of the Lystrosaurus Assemblage Zone, Karoo Basin, predates the end-Permian marine
470 extinction. *Nat. Commun.* 11, 1–8. <https://doi.org/10.1038/s41467-020-15243-7>

471 Glasspool, I.J., Scott, A.C., 2010. Phanerozoic concentrations of atmospheric oxygen reconstructed
472 from sedimentary charcoal. *Nat. Geosci.* 3, 627–630. <https://doi.org/10.1038/ngeo923>

473 Glasspool, I.J., Scott, A.C., Waltham, D., Pronina, N., Shao, L.Y., 2015. The impact of fire on the
474 late Paleozoic Earth System. *Front. Plant Sci.* 6, 1–13. <https://doi.org/10.3389/fpls.2015.00756>

475 Grasby, S.E., Beauchamp, B., Bond, D.P.G., Wignall, P., Talavera, C., Galloway, J.M., Piepjohn, K.,
476 Reinhardt, L., Blomeier, D., 2015. Progressive environmental deterioration in northwestern
477 Pangea leading to the latest Permian extinction. *Geol. Soc. Am. Bull.* 127, 1331–1347.
478 <https://doi.org/10.1130/B31197.1>

479 Grasby, S.E., Beauchamp, B., 2009. Latest Permian to Early Triassic basin-to-shelf anoxia in the
480 Sverdrup Basin, Arctic Canada. *Chem. Geol.* 264, 232–246.
481 <https://doi.org/10.1016/j.chemgeo.2009.03.009>

482 Grasby, S.E., Beauchamp, B., Knies, J., 2016a. Early Triassic productivity crises delayed recovery
483 from world’s worst mass extinction. *Geology* 44, 779–782. <https://doi.org/10.1130/G38141.1>

484 Grasby, S.E., Beauchamp, B., Bond, D.P.G., Wignall, P.B., Sanet, H., 2016b. Mercury anomalies
485 associated with three extinction events (Capitanian Crisis, Latest Permian Extinction and the
486 Smithian/Spathian Extinction) in NW Pangea. *Geol. Mag.* 153, 285–297.
487 <https://doi.org/10.1017/S0016756815000436>

488 Grasby, S.E., Sanei, H., Beauchamp, B., 2011. Catastrophic dispersion of coal fly ash into oceans
489 during the latest Permian extinction. *Nat. Geosci.* 4, 104–107. <https://doi.org/10.1038/ngeo1069>

490 Grasby, S.E., Sanei, H., Beauchamp, B., Chen, Z.H., 2013. Mercury deposition through the
491 Permo-Triassic Biotic Crisis. *Chem. Geol.* 351, 209–216.
492 <https://doi.org/10.1016/j.chemgeo.2013.05.022>

493 Grasby, S.E., Knies, J., Beauchamp, B., Bond, D.P.G., Wignall, P.B., Sun, Y.D., 2019a. Global
494 warming leads to Early Triassic nutrient stress across northern Pangea. *GSA Bull.*

495 <https://doi.org/10.1130/B32036.1>

496 Grasby, S.E., Them, T.R., Chen, Z.H., Yin, R.S., Ardakani, O.H., 2019b. Mercury as a proxy for
497 volcanic emissions in the geologic record. *Earth-Science Rev.* 196, 102880.
498 <https://doi.org/10.1016/j.earscirev.2019.102880>

499 Guo, X.N., Tang, Z.L., Li, W.C., Sheng, J.H., Gao, Y.S., Sun, J.P., Wei, H.X., Ren, J.K., Yang, J.Y.,
500 Li, T.L., Li, H.W., Qiu, G.B., Liang, X.Y., Song, J.J., Guan, Z.M., Li, Y.J., Song, Z.J., Su, X.B.,
501 1991. The late Palaeozoic coal-accumulating laws in Henan province. China University of
502 Geoscience Press, Wuhan, pp. 51-61.

503 Hao, Y.W., Luo, M.S., Xu, Z.L., Zou, Y.R., Tang, T.T., 2014. Division of sedimentary basins and its
504 tectonic evolution in North China from Neoproterozoic to Mesozoic. *Earth Sci. China Univ.*
505 *Geosci.* 39, 1230–1242. <https://doi.org/10.3799/dqkx.2014.106>

506 Hou, J.P., Ouyang, S., 2000. Palynoflora from the Sunjiagou Formation in Liulin County, Shanxi
507 Province. *Acta Palaeontol. Sin.* 39, 356–368.

508 Hu, F.Z., Fu, X.G., Lin, L., Song, C.Y., Wang, Z.W., Tian, K.Z., 2020. Marine Late Triassic-Jurassic
509 carbon-isotope excursion and biological extinction records: New evidence from the Qiangtang
510 Basin, eastern Tethys. *Glob. Planet. Change* 185, 103093.
511 <https://doi.org/10.1016/j.gloplacha.2019.103093>

512 Joachimski, M.M., Lai, X., Shen, S., Jiang, H., Luo, G., Chen, B., Chen, J., Sun, Y., 2012. Climate
513 warming in the latest Permian and the Permian-Triassic mass extinction. *Geology* 40, 195–198.
514 <https://doi.org/10.1130/G32707.1>

515 Li, J.Y., 2006. Permian geodynamic setting of Northeast China and adjacent regions: closure of the
516 Paleo-Asian Ocean and subduction of the Paleo-Pacific Plate. *J. Asian Earth Sci.* 26, 207–224.

517 <https://doi.org/10.1016/j.jseaes.2005.09.001>

518 Liao, Z.W., Hu, W.X., Cao, J., Wang, X.L., Fu, X.G., 2020. Oceanic anoxia through the late Permian
519 Changhsingian stage in the Lower Yangtze region, South China: Evidence from sulfur isotopes
520 and trace elements. *Chem. Geol.* 532, 119371. <https://doi.org/10.1016/j.chemgeo.2019.119371>

521 Liao, Z.W., Hu, W.X., Cao, J., Wang, X.L., Yao, S.P., Wu, H.G., Wan, Y., 2016. Permian-Triassic
522 boundary (PTB) in the Lower Yangtze Region, southeastern China: A new discovery of
523 deep-water archive based on organic carbon isotopic and U-Pb geochronological studies.
524 *Palaeogeogr. Palaeoclimatol. Palaeoecol.* 451, 124–139.
525 <https://doi.org/10.1016/j.palaeo.2016.03.004>

526 Ma, P.F., Wang, L.C., Wang, C.S., Wu, X.H., Wei, Y.S., 2015. Organic-matter accumulation of the
527 lacustrine Lunpola oil shale, central Tibetan plateau: Controlled by the paleoclimate,
528 provenance, and drainage system. *Int. J. Coal Geol.*, 147-148, 58–70. [https://doi.org/](https://doi.org/10.1016/j.coal.2015.06.011)
529 [10.1016/j.coal.2015.06.011](https://doi.org/10.1016/j.coal.2015.06.011)

530 Meyer, K.M., Yu, M., Jost, A.B., Kelley, B.M., Payne, J.L., 2011. $\delta^{13}\text{C}$ evidence that high primary
531 productivity delayed recovery from end-Permian mass extinction. *Earth Planet. Sci. Lett.* 302,
532 378–384. <https://doi.org/10.1016/j.epsl.2010.12.033>

533 Muttoni, G., Gaetani, M., Kent, D.V., Sciunnach, D., Angiolini, L., Berra, F., Garzanti, E., Mattei,
534 M., Zanchi, A., 2009. Opening of the Neo-tethys ocean and the Pangea B to Pangea A
535 transformation during the permian. *GeoArabia* 14, 17–48.
536 [https://doi.org/10.1016/S0012-821X\(03\)00452-7](https://doi.org/10.1016/S0012-821X(03)00452-7)

537 Nan, J.Y., Li, Y.Y., 2004. organic and inorganic carbon-isotope shift and paleoenvironment at the
538 P-T boundary section in Meishan. *Geochimica* 33, 9–19.

539 <https://doi.org/10.3321/j.issn:0379-1726.2004.01.002>

540 Nesbitt, H.W., Young, G.M., 1984. Prediction of some weathering trends of plutonic and volcanic
541 rocks based on thermodynamic and kinetic considerations. *Geochim. Cosmochim. Acta* 48,
542 1523–1534. [https://doi.org/10.1016/0016-7037\(84\)90408-3](https://doi.org/10.1016/0016-7037(84)90408-3)

543 Pan, Z.C., Xu, L., Xi, Y.H., Jia, S.H., 2008. Research on stratigraphic paleontology in Henan
544 province–The Mesozoic. Zhengzhou: The Yellow River Water Conservancy Press. Zhengzhou,
545 pp. 3-33.

546 Rampino, M.R., Rodriguez, S., Baransky, E., Cai, Y., 2017. Global nickel anomaly links Siberian
547 Traps eruptions and the latest Permian mass extinction. *Sci. Rep.* 7, 12416.
548 <https://doi.org/10.1038/s41598-017-12759-9>

549 Ren, J.S., 1987. *Geotectonic evolution of China*. Springer.

550 Retallack, G.J., 2013. Ediacaran gaskiers glaciation of Newfoundland reconsidered. *J. Geol. Soc.*
551 London. 170, 19–36. <https://doi.org/10.1144/jgs2012-060>

552 Roy, D.K., Roser, B.P., 2013. Climatic control on the composition of Carboniferous-Permian
553 Gondwana sediments, Khalaspir basin, Bangladesh. *Gondwana Res.* 23, 1163–1171.
554 <https://doi.org/10.1016/j.gr.2012.07.006>

555 Sanei, H., Grasby, S.E., Beauchamp, B., 2012. Latest Permian mercury anomalies. *Geology* 40, 63–
556 66. <https://doi.org/10.1130/G32596.1>

557 Scott, A.C., 2000. The Pre-Quaternary history of fire. *Palaeogeogr. Palaeoclimatol. Palaeoecol.* 164,
558 281–329. [https://doi.org/10.1016/S0031-0182\(00\)00192-9](https://doi.org/10.1016/S0031-0182(00)00192-9)

559 Shang, G.X., 1997. *The late Paleozoic coal geology of North China Platform, Taiyuan: Shanxi*
560 Science and Technology Press, Taiyuan, pp. 1-160.

561 Shen, J., Algeo, T.J., Hu, Q., Zhang, N., Zhou, L., Xia, W.C., Xie, S.C., Feng, Q.L., 2012. Negative
562 C-isotope excursions at the Permian-Triassic boundary linked to volcanism. *Geology* 40, 963–
563 966. <https://doi.org/10.1130/G33329.1>

564 Shen, J., Schoepfer, S.D., Feng, Q.L., Zhou, L., Yu, J.X., Song, H.Y., Wei, H.Y., Algeo, T.J., 2015.
565 Marine productivity changes during the end-Permian crisis and Early Triassic recovery.
566 *Earth-Science Rev.* 149, 136–162. <https://doi.org/10.1016/j.earscirev.2014.11.002>

567 Shen, J., Yu, J.X., Chen, J.B., Algeo, T.J., Xu, G.Z., Feng, Q.L., Shi, X., Planavsky, N.J., Shu, W.C.,
568 Xie, S.C., 2019. Mercury evidence of intense volcanic effects on land during the
569 permian-triassic transition. *Geology* 47, 1117–1121. <https://doi.org/10.1130/G46679.1>

570 Shen, S.Z., Cao, C.Q., Zhang, H., Bowring, S.A., Henderson, C.M., Payne, J.L., Davydov, V.I.,
571 Chen, B., Yuan, D.X., Zhang, Y.C., Wang, W., Zheng, Q.F., 2013. High-resolution $\delta^{13}\text{C}_{\text{carb}}$
572 chemostratigraphy from latest Guadalupian through earliest Triassic in South China and Iran.
573 *Earth Planet. Sci. Lett.* 375, 156–165. <https://doi.org/10.1016/j.epsl.2013.05.020>

574 Shen, S.Z., Crowley, J.L., Wang, Y., Bowring, S.A., Erwin, D.H., Sadler, P.M., Cao, C.Q., Rothman,
575 D.H., Henderson, C.M., Ramezani, J., Zhang, H., Shen, Y., Wang, X.D., Wang, W., Mu, L., Li,
576 W.Z., Tang, Y.G., Liu, X.L., Liu, L.J., Zeng, Y., Jiang, Y.F., Jin, Y.G., 2011. Calibrating the
577 end-Permian mass extinction. *Science* 334, 1367–1372. <https://doi.org/10.1126/science.1213454>

578 Shen, S.Z., Zhang, H., Zhang, Y.C., Yuan, D.X., Chen, B., He, W.H., Mu, L., Lin, W., Wang, W.Q.,
579 Chen, J., Wu, Q., Cao, C.Q., Wang, Y., Wang, X.D., 2019. Permian integrative stratigraphy and
580 timescale of China. *Sci. China Earth Sci.* 62, 154–188.
581 <https://doi.org/10.1007/s11430-017-9228-4>

582 Sun, H., Xiao, Y.L., Gao, Y.J., Zhang, G.J., Casey, J.F., Shen, Y.N., 2018. Rapid enhancement of

583 chemical weathering recorded by extremely light seawater lithium isotopes at the
584 Permian-Triassic boundary. *Proc. Natl. Acad. Sci. U. S. A.* 115, 3782–3787.
585 <https://doi.org/10.1073/pnas.1711862115>

586 Sun, Y.D., Joachimski, M.M., Wignall, P.B., Yan, C.B., Chen, Y.L., Jiang, H.S., Wang, L.N., Lai,
587 X.L., 2012. Lethally hot temperatures during the early triassic greenhouse. *Science* 338, 366–
588 370. <https://doi.org/10.1126/science.1224126>

589 Sun, Y.D., Wignall, P.B., Joachimski, M.M., Bond, D.P.G., Grasby, S.E., Lai, X.L., Wang, L.N.,
590 Zhang, Z.T., Sun, S., 2016. Climate warming, euxinia and carbon isotope perturbations during
591 the Carnian (Triassic) Crisis in South China. *Earth Planet. Sci. Lett.* 444, 88–100.
592 <https://doi.org/10.1016/j.epsl.2016.03.037>

593 Sun, Y.D., Zulla, M.J., Joachimski, M.M., Bond, D.P.G., Wignall, P.B., Zhang, Z.T., Zhang, M.H.,
594 2019. Ammonium ocean following the end-Permian mass extinction. *Earth Planet. Sci. Lett.*
595 518, 211–222. <https://doi.org/10.1016/j.epsl.2019.04.036>

596 Thiry, M., 2000. Palaeoclimatic interpretation of clay minerals in marine deposits: An outlook from
597 the continental origin. *Earth Sci. Rev.* 49, 201–221.
598 [https://doi.org/10.1016/S0012-8252\(99\)00054-9](https://doi.org/10.1016/S0012-8252(99)00054-9)

599 Van Soelen, E.E., Twitchett, R.J., Kürschner, W.M., 2018. Salinity changes and anoxia resulting
600 from enhanced run-off during the late Permian global warming and mass extinction event. *Clim.*
601 *Past* 14, 441–453. <https://doi.org/10.5194/cp-14-441-2018>

602 Wang, R.N., 1997. New Advance of the Study of the Shiqianfeng Formation in Western Henan. *Geol.*
603 *Rev.* 43, 200–209.

604 Wang, Z.Q., Chen, A. S., 2001. Traces of arborescent lycopsids and dieback of the forest vegetation

605 in relation to the terminal Permian mass extinction in North China. *Rev. Palaeobot. Palynol.* 117,
606 217–243. [https://doi.org/10.1016/S0034-6667\(01\)00094-X](https://doi.org/10.1016/S0034-6667(01)00094-X)

607 Wang, Z.Q, Wang, L., 1986. Late Permian fossil plants from the lower part of the Shiqianfeng
608 (Shihchienfeng) group in North China. *Bull. Tianjin Inst. Geol.Min.Res.No.* 15, 1–80.

609 Wignall, P.B., Chu, D.L., Hilton, J., Dal Corso, J., Wu, Y.Y., Wang, Y., Atkinson, J., Tong, J.N.
610 2020. Death in the Shallows: the record of Permo-Triassic mass extinction in paralic settings,
611 southwest China. *Glob. Planet. Change* <https://doi.org/10.1016/j.gloplacha.2020.103176>.

612 Wignall, P.B., Hallam, A., 1992. Anoxia as a cause of the Permian/Triassic mass extinction: facies
613 evidence from northern Italy and the western United States. *Palaeogeogr. Palaeoclimatol.*
614 *Palaeoecol.* 93, 21–46. [https://doi.org/10.1016/0031-0182\(92\)90182-5](https://doi.org/10.1016/0031-0182(92)90182-5)

615 Wignall, P.B., Twitchett, R.J., 1996. Oceanic Anoxia and the End Permian Mass Extinction. *Science*
616 272, 1155–1158. <https://doi.org/10.1126/science.272.5265.1155>

617 Winguth, A., Winguth, C., 2013. Precession-driven monsoon variability at the Permian-Triassic
618 boundary - Implications for anoxia and the mass extinction. *Glob. Planet. Change* 105, 160–170.
619 <https://doi.org/10.1016/j.gloplacha.2012.06.006>

620 Wu, Y., Fan, T.L., Jiang, S., Yang, X.Q., 2017. Lithofacies and sedimentary sequence of the lower
621 Cambrian Niutitang shale in the upper Yangtze platform, South China. *J. Nat. Gas Sci. Eng.* 43,
622 124–136. <https://doi.org/10.1016/j.jngse.2017.04.002>

623 Xie, S.C., Pancost, R.D., Huang, J.H., Wignall, P.B., Yu, J.X., Tang, X.Y., Chen, L., Huang, X.Y.,
624 Lai, X.L., 2007. Changes in the global carbon cycle occurred as two episodes during the
625 Permian-Triassic crisis. *Geology* 35, 1083–1086. <https://doi.org/10.1130/G24224A.1>

626 Yang, G.X., Wang, H.S., 2012. Yuzhou Flora-A hidden gem of the Middle and Late Cathaysian

627 Flora. *Sci. China Earth Sci.* 55, 1601–1619. <https://doi.org/10.1007/s11430-012-4476-2>

628 Yang, Q., Lei, S., 1987. *Depositional Environments and Coal-forming Characteristics of Late*

629 *Palaeozoic Coal Measures in Yuxian, Henan Province*, Beijing: Geological Publishing House.

630 Yin, H.F., Song, H.J., 2013. Mass extinction and Pangea integration during the Paleozoic-Mesozoic

631 transition. *Sci. China Earth Sci.* 56, 1791–1803. <https://doi.org/10.1007/s11430-013-4624-3>

632 Zhang, G.W., Meng, Q.R., Lai, S.C., 1995. Tectonics and structure of Qinling orogenic belt. *Sci.*

633 *China Chem.* 38, 1379–1394. <https://doi.org/10.1007/BF00696740>

634 Zhang, H., Cao, C.Q., Liu, X.L., Mu, L., Zheng, Q.F., Liu, F., Xiang, L., Liu, L.J., Shen, S.Z., 2016.

635 The terrestrial end-Permian mass extinction in South China. *Palaeogeogr. Palaeoclimatol.*

636 *Palaeoecol.* 448, 108–124. <https://doi.org/10.1016/j.palaeo.2015.07.002>

637 Zhao, Y., Zhai, M.G., Chen, H., Zhang, S.H., 2017. Paleozoic-early Jurassic tectonic evolution of

638 North China Craton and its adjacent orogenic belts. *Geol. China* 44, 44–60.

639 <https://doi.org/10.12029/gc20170104>

640 Zhang, S.H., Zhao, Y., Ye, H., Liu, J. M., Hu, Z.C., 2014. Origin and evolution of the Bainaimiao

641 arc belt: Implications for crustal growth in the southern Central Asian orogenic belt. *Geol. Soc.*

642 *Am. Bull.* 126, 1275–1300. <https://doi.org/10.1130/B31042.1>

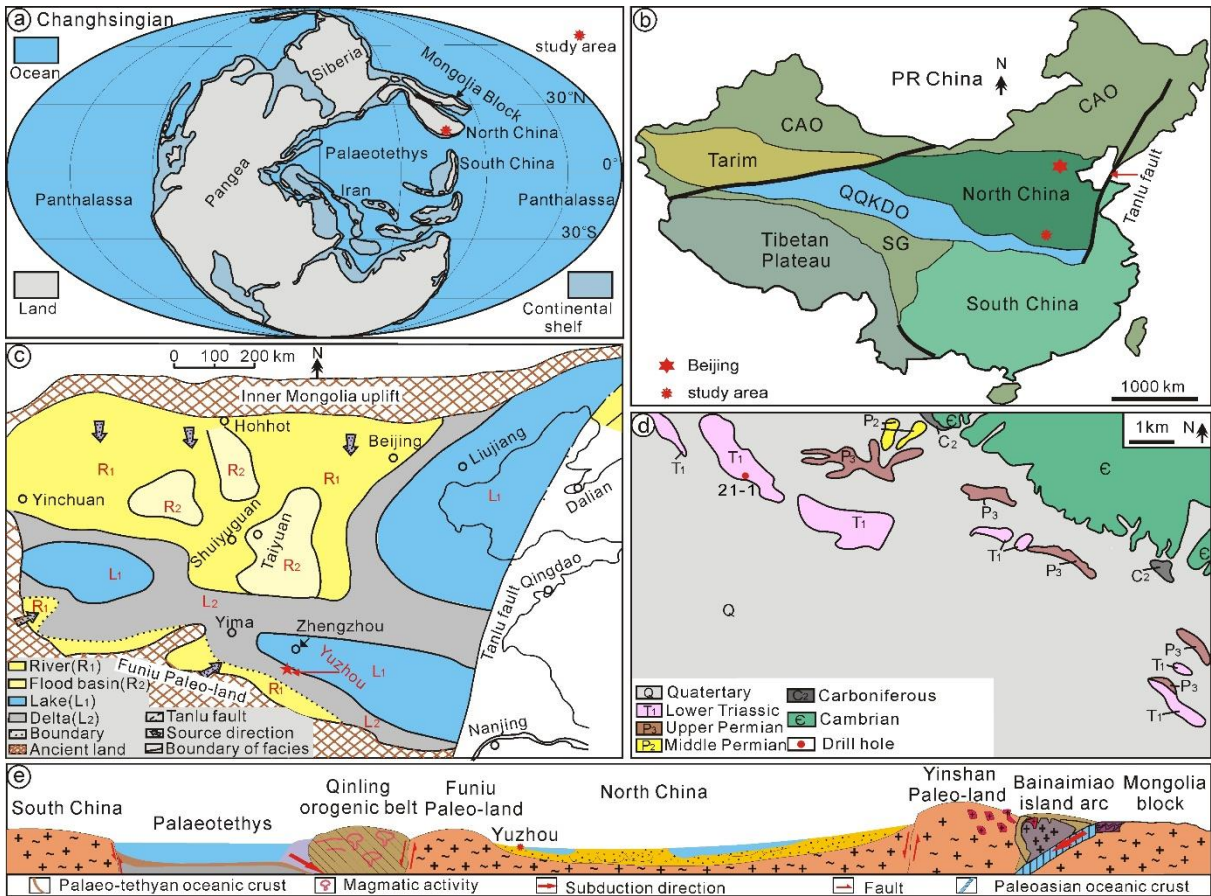
643 Ziegler, A.M., Hulver, M.L., Rowley, D.B., 1997. Permian world topography and climate, in: *Late*

644 *Glacial and Postglacial Environmental Changes: Quaternary, Carboniferous-Permian and*

645 *Proterozoic*. Oxford Univ Press, pp. 111–146.

646 **Figure captions**

647



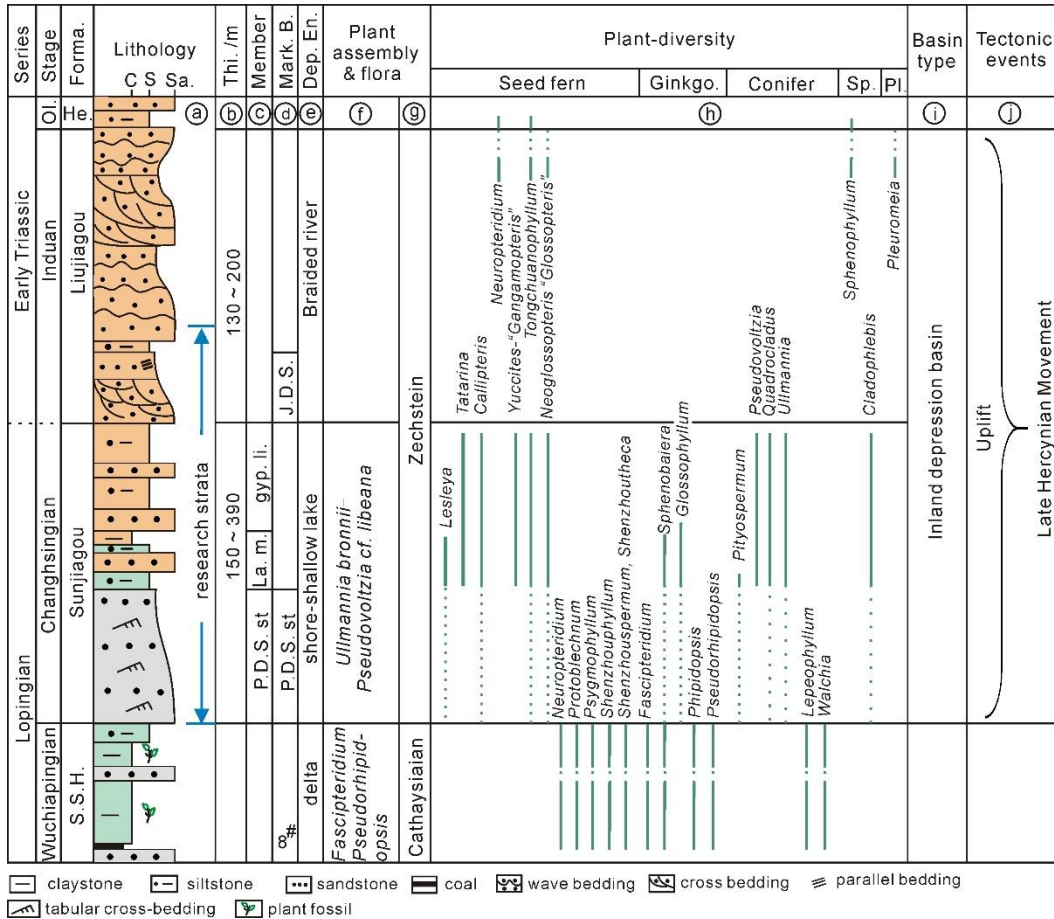
648

649 Figure 1. Location and geological context for the study area. **a**, Paleogeographic reconstruction for
 650 the Lopingian (late Permian) showing location of North China Plate (modified from Ziegler et al.,
 651 1997); **b**, Generalized tectonic map of present-day China showing the location of the North China
 652 Plate and the study area (modified from Ren, 1987), Abbreviations: CAO = Central Asian Orogen;
 653 SG = Songpan-Ganzi; QQKDO = Qinling-Qilian-Kunlun-Dabie Orogen; **c**, Paleofacies map of the
 654 North China Plate during the Changhsingian (Sunjiagou Formation) showing the location of study
 655 area (modified from Shang, 1997), Abbreviations: R1= river; L1= lake; L2= delta; **d**, Local
 656 geological map of the Yuzhou coalfield showing the locations of the borehole core sections in the
 657 study area, Abbreviations: Q=Quaternary; L1=Lower Triassic; P3=Upper Permian; P2=Middle
 658 Permian; C2= Carboniferous; E= Cambrian, and the number represents drill hole number, e.g., 21-1;
 659 **e**, Schematic diagram showing the basin-mountain relationships and the location of the North China

660 Plate during the Lopingian (modified from Shang, 1997; Zhao et al., 2017).

661

662

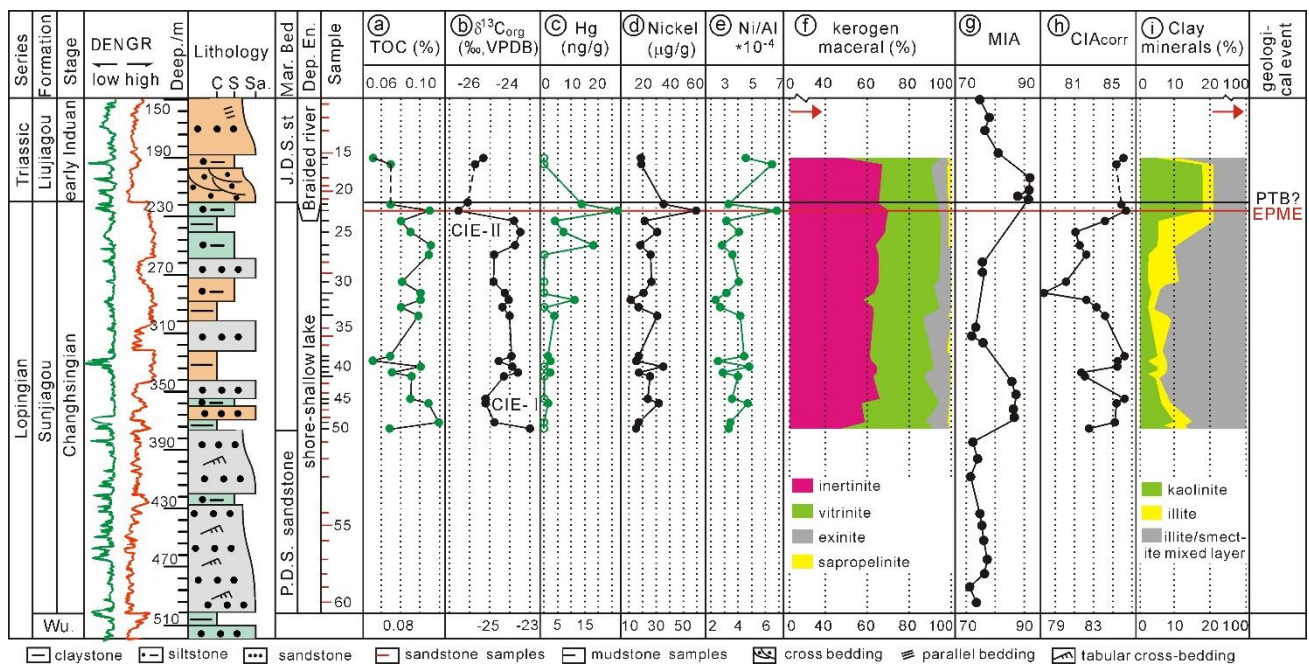


663

664 Figure 2. Stratigraphic framework for the Permian-Triassic boundary strata from the Yuzhou
 665 coalfield. Note: Lithology from Yang and Lei (1987) and the colors filling in lithology are similar to
 666 that of the rocks. **a**, Strata in the basin highlighting the study interval; **b**, Formation thicknesses from
 667 Guo et al. (1991) and Pan et al. (2008); **c**, Stratigraphic division of the Sunjiagou Formation from
 668 Yang and Lei (1987) and Wang (1997); **d**, Marker beds from Guo et al. (1991); **e**, Summary
 669 sedimentary environments from Guo et al. (1991); **f**, Fossil plant assemblages from Yang and Wang
 670 (2012); **g**, Floral provinces from Wang and Wang (1986), Pan et al. (2008) and Yang and Wang
 671 (2012); **h**, Vertical distribution of plant fossils from Chu et al. (2015) showing the extinction near the
 672 boundary of the Sunjiagou and Liujigou formations; **i**, Basin type from Hao et al. (2014); **j**,

673 Tectonic events from Shang (1997) and Zhao et al. (2017). Abbreviations: Ol. = Olenekian; Forma. =
 674 Formation; He. = Heshanggou; S.S.H. = Shangshihezi; C = Clay; S = Siltstone; Sa. = Sandstone; Thi.
 675 = Thick; Mark. B. = Marker bed; 8# = 8# coal seams; P.D.S.st: Pingdingshan sandstone; La. m.:
 676 Lamellibranchiate marl; Gyp. Li.: Gypsum lime-nodule; J.D.S.: Jindoushan Sandstone; Dep. En. =
 677 Depositional environment; Sporo. = Sporo-pollen; *Ginkgo.*: Ginkgopsida; Sp.: Sphenopsida; Pl.:

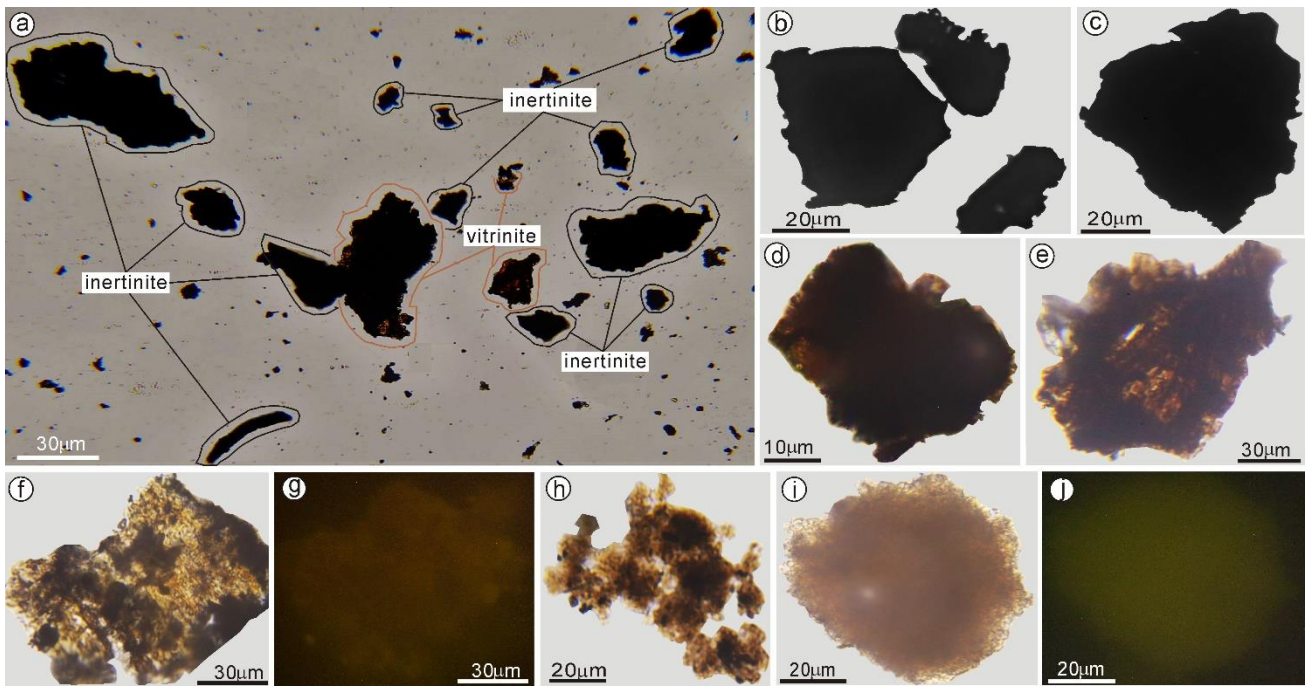
678



679

680 Figure 3. Change in value of TOC, $\delta^{13}C_{org}$, Hg and nickel concentrations, kerogen macerals, MIA
 681 and CIA, and clay minerals component in the study area. Note: the colors filling in lithology are
 682 similar to that of rocks, the interpretation of the deposition environment is from Guo et al. (1991) and
 683 Pan et al. (2008), and pay attention to the scales in column f and i. Abbreviations: C = claystone; S =
 684 siltstone; Sa. = sandstone; Mark. Bed = marker bed; Dep. En. = depositional environment; J.D.S st =
 685 Jindoushan Sandstone; P.D.S. sandstone = Pingdingshan sandstone; PTB = Permian-Triassic
 686 boundary; EPME = End Permian mass extinction.

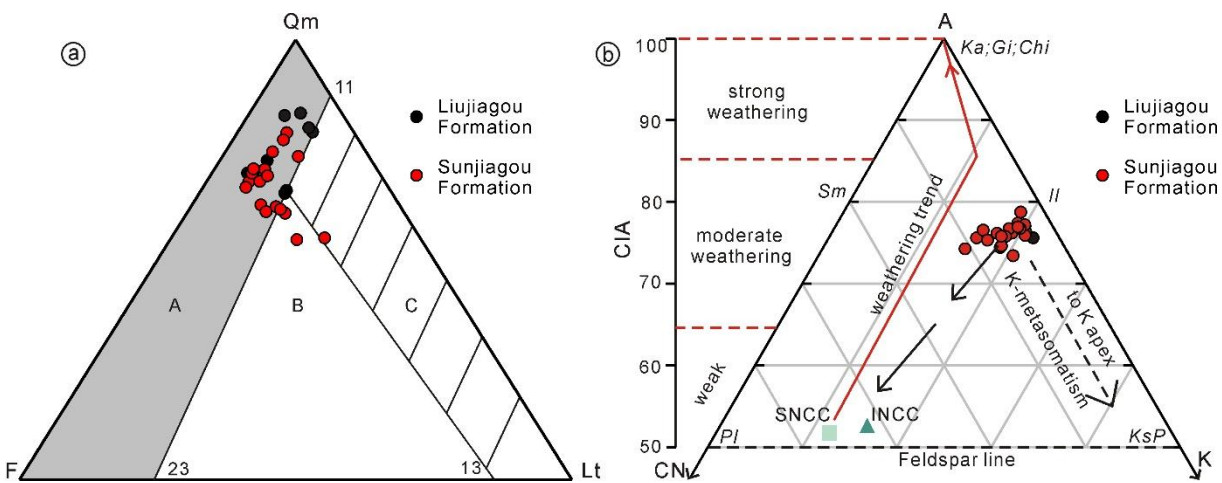
687



688

689 Figure 4. Photomicrographs showing microstructure characteristics of kerogen macerals in the study
 690 area. **a**, overview showing characteristics of kerogen macerals (transmitted light, sample #23); **b** and
 691 **c**, fusinite (transmitted light, #45); **d** and **e**, vitrinite (transmitted light, sample #16 and #49); **f** and **g**,
 692 suberinite (transmitted light and fluorescence, respectively, sample #42); **h**, saproelinite
 693 (transmitted light, sample #22); **i** and **j**, saproelinite (transmitted light and fluorescence, respectively,
 694 sample #50)

695

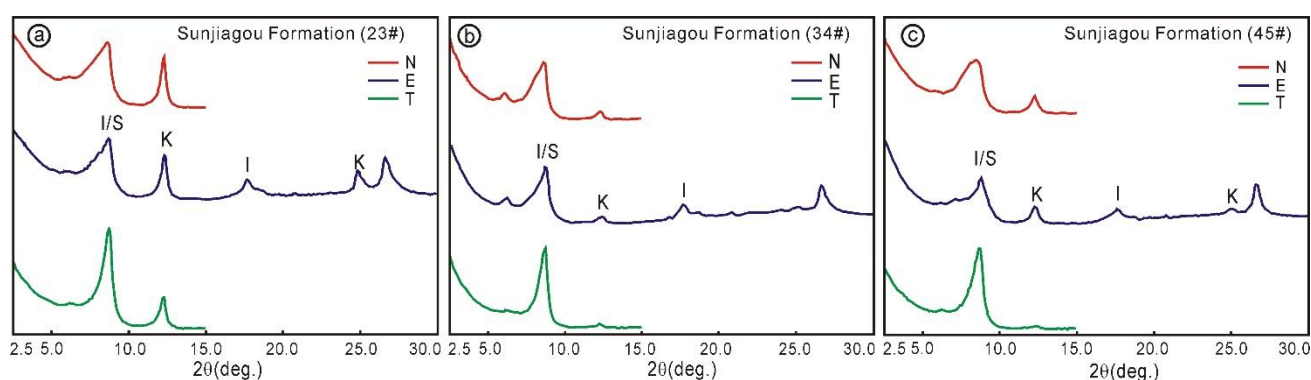


696

697 Figure 5. Qm-F-Lt diagram of sandstone and A-CN-K diagram of mudstone in the study area. **a**,
 698 Qm-F-Lt diagram of sandstone samples from Changhsingian to early Induan showing the main

699 provenance area of continental block (modified from Dickinson, 1985). Abbreviations: Qm =
700 monocrystalline quartz; F = feldspar (plagioclase + K-feldspar); Lt = total lithics (lithics +
701 polycrystalline quartz); A = Continental block; B = Magmatic arc; C = Recycled orogen. **b**, A-CN-K
702 diagram of mudstone samples from Changhsingian to early Induan with the chemical index of
703 alteration (CIA) scale to the left, showing the possible influence of Potassium metasomatism. For
704 comparison, the average upper crust CIA value of southern and interior North China Craton are
705 shown (modified from Cao et al., 2019). Abbreviations: A = Al₂O₃; CN = CaO*+Na₂O; K = K₂O;
706 CIA= chemical index of alteration; Ka = kaolinite; Gi = gibbsite; Il = illite; PI = Plagioclase; Chl =
707 chlorite; Sm = smectite; Ksp = K-feldspar; INCC = Interior North China Craton; SNCC = Southern
708 North China Craton.

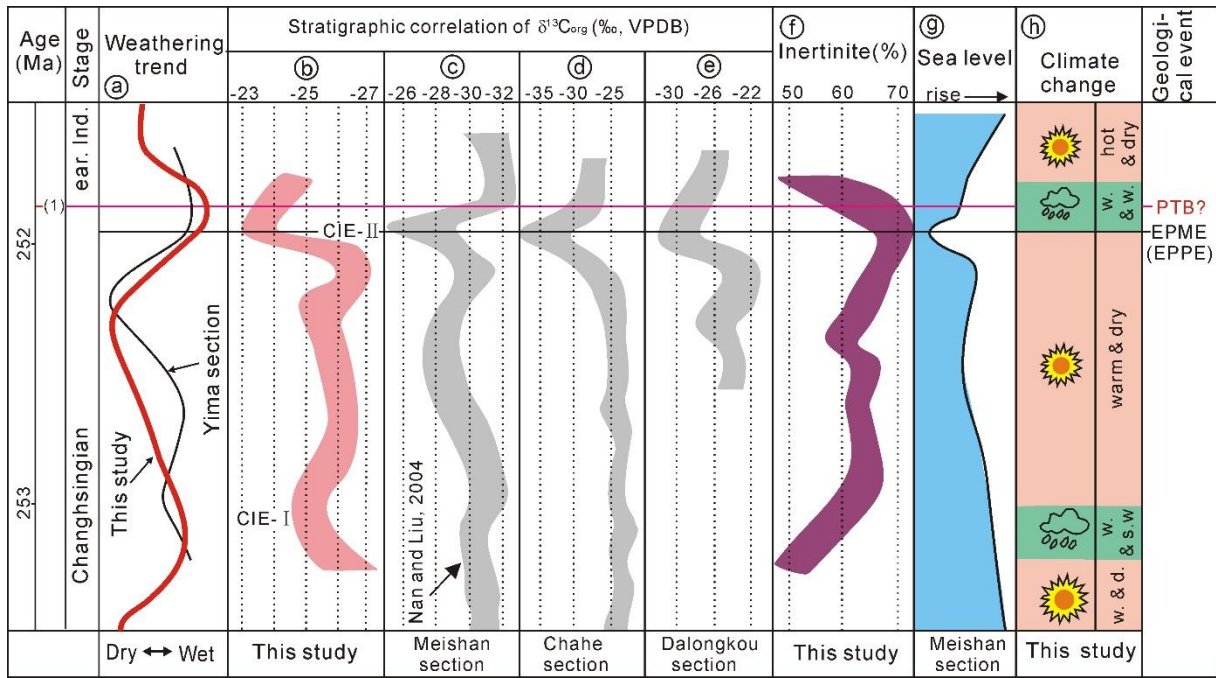
709



710

711 Figure 6. X-ray diffraction (XRD) patterns of clay fractions of typical samples in the study area. N, E
712 and T designate spectra of a naturally-oriented slide, ethylene-glycol saturated for oriented slide and
713 high-temperature treated at 450°C for oriented slide, respectively. **a**, XRD patterns showing high
714 content of illite-smectite mix layer and kaolinite (Sunjiagou Formation, sample #23); **b**, XRD
715 patterns showing high content of illite-smectite mix layer and lowest kaolinite content (Sunjiagou
716 Formation, sample #34); **c**, XRD patterns showing high content of illite-smectite mix layer and less
717 kaolinite content (Sunjiagou Formation, sample #45). Abbreviations: I/S = illite-smectite mixed layer;
718 K = kaolinite; I = illite.

719



721

722

723

724

725

726

727

728

729

730

731

732

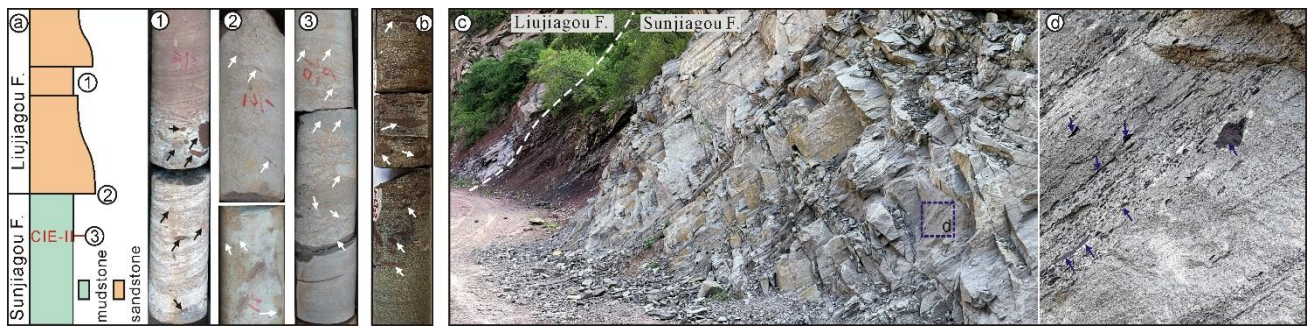
733

734

735

736

Figure 7. Comparison among weathering trend, carbon isotope records, inertinite content, sea-level, and the paleoenvironment events from Changhsingian to early Induan. Age stratigraphic framework from Shen S. et al. (2019); (1) represents P-T boundary age: $251.902 \pm 0.024\text{Ma}$; **a**, red curve represent a weathering trend by MIA and CIA in the study area, and the black curve represent a weathering trend by CIA in Yima section (southern NCP) near the study area (Cao et al., 2019); **b**, vertical change trend of $\delta^{13}C_{org}$ in the study area showing two negative isotope excursions near the middle and end of the Changhsingian; **c**, **d** and **e**, $\delta^{13}C_{org}$ from the marine (Meishan) and terrestrial (Chahe and Dalongkou) sections by Nan and Liu (2004), Zhang et al. (2016) and Shen J et al. (2019); **f**, inertinite content from the present study; **g**, sea-level curve (relative to current sea level) of the Meishan section from Cao et al. (2009); **h**, paleoclimate change inferred from clay mineral component, CIA and MIA. Abbreviations: ear. Ind. = early Induan; w. & d. = warm & dry; w. & s. w. = warm & slight wet; w. & w. = warm & wet; PTB = Permian-Triassic boundary; EPME = End Permian mass extinction; EPPE = End Permian plant extinction.



739 Figure 8. Pictures showing a lot of mudstone clastics was observed in uppermost Sunjiagou
 740 Formation in NCP. **a**: lots of greyish-green and purplish-red mudstone clastics occur in the lake
 741 mudstone associated with the CIE-II and last into early Triassic in the drill core ZK21-1, Henan
 742 province (southern NCP). Note: the colors filling in lithology are similar to that of rocks, and the
 743 numbers (e.g.,(1)-(3)) represent the vertical order of lithology. **b**: lots of mudstone clastics was
 744 observed in the uppermost Sunjiagou Formation in borehole core profile in Liujiang area, Hebei
 745 province (middle NCP). **c**: Picture of Shuiyuguan section (Shaanxi province, middle NCP) showing
 746 the boundary of Sunjiagou and Liujiagou formations with highlighted box enlarged in **d**. **d**:
 747 enlargement from **c** showing details of mudstone clastics in the uppermost Sunjiagou Formation.